Experimental and numerical studies on the structural response of normal strength concrete slabs subjected to blast loading

Martin Kristoffersen[a,*], Jon Eide Pettersen[a,b], Vegard Aune[a,b], Tore Børvik[a,b]

[a] *Structural Impact Laboratory (SIMLab), Department of Structural Engineering, Norwegian University of Science and Technology (NTNU), Rich. Birkelands vei 1A, NO-7491 Trondheim, Norway*
[b] *Centre for Advanced Structural Analysis (CASA), NTNU NO-7491 Trondheim, Norway*

Abstract

To assess the blast performance of concrete structures, a shock tube has been used to simulate blast loading against concrete slabs of two different mixes ordered as C45/55 and C20/25. The C45/55 slabs were tested without reinforcement, whereas the C20/25 slabs were tested both with and without reinforcement to investigate the effect of adding steel bars on the structural response. The performance of the shock tube itself was also evaluated. Compression tests on cubes and cylinders of both concrete recipes were performed to obtain material input data for numerical simulations. Numerous compression tests were also conducted using the C20/25 mix to obtain insights into the statistical variation in the material properties as concrete is inherently heterogeneous at the macroscopic level. In addition, tensile splitting tests were conducted on both materials. The shock tube tests show that the boundary conditions are important and that the reinforcement will direct the crack pattern. Fluid-structure interaction (FSI) effects are not dominant for this particular problem, because the concrete slabs suffer relatively small deformations before through-thickness cracks appear. Once cracks extend through the thickness, FSI effects may become influential, but it appears that when this occurs there is little or no residual capacity left in the slabs. Numerical simulations were used to investigate the influence of various parameters, revealing that the results are highly dependent on the boundary conditions and particularly on the tensile strength of the concrete. It was found necessary to model the entire clamping assembly to recreate the experimental observations.

Keywords: Shock tube, blast loading, concrete slabs, digital image correlation, numerical simulations

1. Introduction

Concrete is one of the most widely used construction materials, and due to its versatility in shape and form, relatively low price, structural properties and abundance, it will continue to be so for the foreseeable future. However, the low tensile strength of concrete warrants the use of steel reinforcement. One of the most recent ideas for using reinforced concrete is for submerged floating tunnels (SFT) [1], a concept deemed viable by several feasibility studies [2, 3]. Although analyses of such structures have been performed [4–6], no such structure has ever been built in full-scale. As a part of the project that aims to make the Norwegian coastal highway route E39 ferry-free [7], an SFT has been suggested as a means of crossing some deep and wide fjords. One of the concerns for an SFT is the case of an accidental explosion inside the tunnel, for instance, from a collision involving a tanker carrying flammable goods. Naturally, one cannot perform a full-scale test of such a massive construction, thus, one has to utilise smaller components and finite element (FE) simulations. This study aims to investigate the behaviour of concrete slabs subjected to extreme loading conditions of the type arising from a blast load. A shock tube facility [8] has been used to generate the load on the

*Corresponding author, tel.: +47-73-59-46-87; fax: +47-73-59-47-01
Email address: martin.kristoffersen@ntnu.no (Martin Kristoffersen)

slabs, and an important part of this study is to assess the test rig's performance and suitability for use with concrete specimens and assess the qualitative performance of FE models.

With blast loading due to terrorist attacks also being an increased concern [9], expanding the database of experimental results in this field is important – both to obtain a better understanding of a structure's behaviour due to such loads, and for the verification and validation of numerical models aimed at handling this complex problem. The seminal work by Kingery and Bulmash [10] has been essential for determining load parameters, and has naturally been used in several studies [11–14]. A more general review of blast loaded plates can be found in the work by Rajendran and Lee [15].

Concrete slabs subjected to blast loading have been increasingly studied with various approaches [16–19]. Full-scale field tests on concrete slabs have been conducted by Schenker et al. [20], who found that aluminium foam added to the concrete structure may have positive blast mitigation properties. Fibre-reinforced concrete is typically used for that purpose [21, 22], and even the aggregate can be augmented to that end [23]. Retrofitting concrete slabs with fibre-reinforced concrete may also improve the structure's blast performance [24]. Fibres can also improve the capacity of columns exposed to blast loading [25, 26]. This naturally applies to slabs as well [27], but conventional reinforcement is still important for the post-blast static behaviour [22]. A review of fibre-reinforced concrete subjected to dynamic loading has been performed by Soufeiani et al. [28].

The shock tube technique is a well-established approach used to simulate blast loading against structures [29, 30]. The appeal of shock tube experiments rather than using explosives – where even the charge orientation may influence the results [31] – is that the produced loads are consistent and the boundary conditions are well defined. Toutlemonde et al. [32] considered shock tube testing of concrete slabs to be a realistic structural test that can be used to validate e.g. design codes. Further testing of simply supported concrete slabs [33] showed that rapid loading may trigger a shear mechanism rather than bending, which could cause earlier failure compared with quasi-static bending. One-way slabs made from different types of concrete with various reinforcements were tested by Thiagarajan et al. [34] and replicated numerically, where mesh sensitivity proved to be an important issue when concrete is exposed to extreme dynamic loading conditions. Concrete structures exhibit a sensitivity to the load rate, a topic that is highly studied and debated [35–42]. An investigation into rate effects in concrete is beyond the scope of the current study, although it will be mentioned in the context of blast loading.

This study consists of an experimental part and a numerical part. The main experimental objective is to determine the blast load capacity of concrete slabs using a shock tube. Two different concrete mixes ordered as C45/55 and C20/25 were used to cast slabs, where the former mix was tested without reinforcement, and the latter was tested both with and without reinforcement. An estimate of the pressure at which the slabs suffer through-thickness cracks is made for the different material configurations. A battery of standard concrete material tests were carried out to verify that the concrete mixes possessed the mechanical properties as ordered. Potential fluid-structure interaction (FSI) effects during shock loading and the effects of boundary conditions are discussed, and the use of 3D digital image correlation (3D-DIC) as a deformation measurement tool is assessed. The shock tube as a means of generating blast loads against concrete components was also verfied. The experiments are captured using two Phantom v1610 high-speed cameras which are synchronised with the pressure recordings in the shock tube.

Finally, the numerical part of this study investigates to what extent a standard commercial FE software (LS-DYNA [43]) is able to reproduce the experimental results. The K&C model [44, 45] was chosen based on its ease of use and applicability to model blast load scenarios [17, 31, 34, 46]. Different ways of modelling the boundary conditions were evaluated, and the effects of altering different material parameters were studied. In general, the numerical simulations gave good qualitative results.

2. Material testing

2.1. Concrete

A list of the main constituents in the concrete mixes ordered as C45/55 and C20/25 is presented in Table 1. A set of common quasi-static concrete tests (cube compression, cylinder compression and tensile splitting) was conducted to assess the mechanical material properties of the two concrete materials. Cubes with side length 100 mm were used, while the cylinders were 100 mm in diameter and 200 mm in length. The compression tests were carried out in a fully automated Toni Tech 3000 kN load controlled apparatus (load rate 0.8 MPa/s), while the tensile splitting tests were

Table 1: Constituents of concrete recipes given in weight percentage.

Concrete mix	Water	Cement	w/c ratio	Aggr. 0-8 mm	Aggr. 8-16 mm	Total
C45/55	7.4 %	19.3 %	0.387	43.1 %	30.2 %	100.0 %
C20/25	8.0 %	12.9 %	0.621	50.1 %	29.0 %	100.0 %

performed in a Mohr/Federhaft/Losenhausen BP-300 compression rig (load rate 0.6 MPa/s). The tests provided the cube compressive strength f_c, the cylinder compressive strength f_{cc}, and the estimated tensile strength f_t based on the design code [47]. The mass densities ρ_c were also measured. Each test was repeated three times, except for the tests on the C20/25 concrete which was repeated 20 times (after 28 days of curing).

Table 2 lists the average values and standard deviation from the tests. The results show that the concrete ordered as C45/55 meets the requirements for the classification. For the C20/25 concrete, the cylinder and cube compressive strengths were 39.6 MPa and 46.3 MPa, respectively. A more accurate classification would be C30/37 according to [48], so this result shows that what is ordered is not necessarily what is received and underscores the importance of conducting material tests. For consistency throughout the study, the initial denomination (C20/25) has been retained for this concrete mix.

Table 2: Average values and standard deviation from material tests on concrete. Subscript numbers indicate days of curing

Concrete mix	$f_{c,28}$ [MPa]	$f_{c,40}$ [MPa]	$f_{cc,28}$ [MPa]	$f_{t,28}$ [MPa]	$\rho_{c,28}$ [kg/m^3]
C45/55	64.8 ± 0.8	68.4 ± 0.8	54.9 ± 0.5	4.1 ± 0.3	$2\,360 \pm 11$
C20/25	46.3 ± 0.7	49.1 ± 0.3	$39.6 \pm 0.7^*$	$3.5 \pm 0.3^*$	$2\,445 \pm 9$

*Tested 29 days after casting due to lab schedule.

2.2. *Steel*

The steel reinforcement used herein is a standard off-the-shelf grid of smooth circular steel bars (initial diameter $D_0 = 2.6$ mm) connected with spot welds at centre offsets of approximately 72 mm in both directions, thereby forming a regular quadratic net. In total, 12 specimens used for tension tests were cut from the net – 6 in each direction of the net. Two of the 12 specimens (one from each direction) were cut such that the weld became part of the gauge area during testing, while the remaining 10 specimens were cut from between the welds.

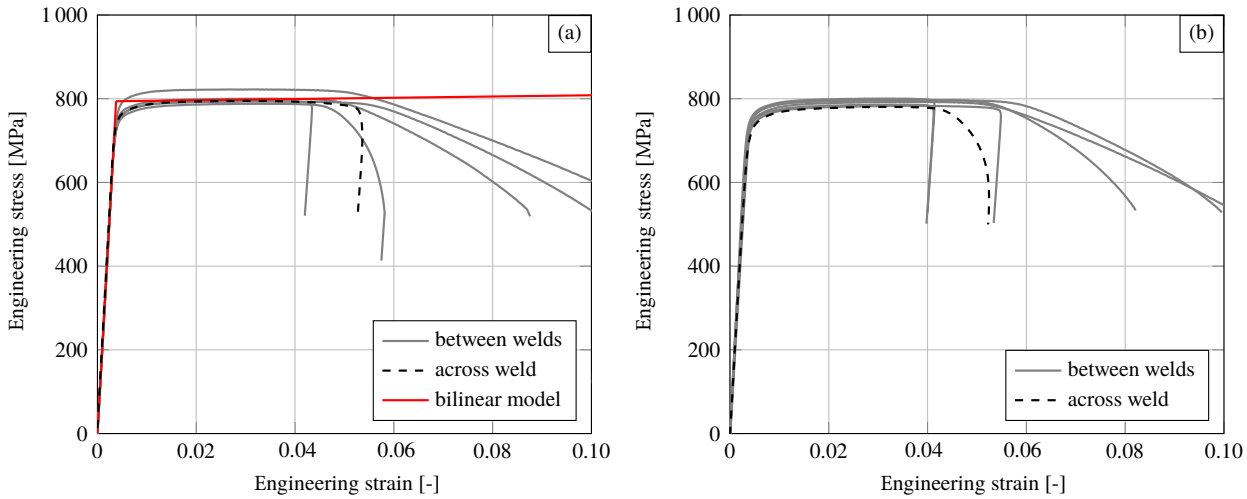

Fig. 1: Tension test results of steel reinforcement in (a) direction 0° and (b) direction 90°.

Engineering stress and engineering strain from quasi-static (estimated initial strain rate of $3.6 \cdot 10^{-4}$ s^{-1}) tension tests on the steel bars are plotted in Fig. 1, with the specimens from the 0° direction to the left and those from the 90° direction to the right. Included in Fig. 1(a) is the bilinear material model used for the reinforcement in the numerical simulations in Section 4. The average yield stress defined as the stress at 0.2% plastic strain, and its standard deviation, were calculated to be 766.4±13.6 MPa. Based on the tension tests, Young's modulus was calculated to be 210 277 ± 9 669 MPa. The fracture strain ε_f after testing was obtained by measuring the diameter D_f at the root of the neck, enabling the calculation of $\varepsilon_f = 2\ln\left(D_0/D_f\right)$ – which resulted in $\varepsilon_f = 0.880 \pm 0.041$.

3. Component tests

A shock tube facility was used to test concrete slabs cast from the C45/55 and C20/25 concretes described above. In addition to assessing the performance of the shock tube, a main objective was to observe how the slabs behaved when exposed to increasing shock loads, as well as to estimate the overpressure at which through-thickness cracks appear. For the C20/25 concrete, reinforcement was added to some of the slabs to determine the influence of adding steel bars on the crack pattern and deformation. The reinforcement grids were placed with an approximately 7 mm offset from each surface, making the distance between their centres approximately 36 mm.

To maintain good control of the geometry, the concrete slabs were cast in a custom-made wooden mould (see Fig. 2) designed according to the shock tube dimensions, as suggested by Toutlemonde et al. [32]. Smooth lubricated plastic tubes were inserted through the bolt holes to secure a proper shape and to align the cutouts. When including the reinforcement, some of the reinforcement bars were cut to accommodate the plastic tubing. The mould and plastic tubing were removed two days after casting, and the slabs were then stored in moist burlap sacks at room temperature to provide good curing conditions. A reinforcement bar looping on the outside of the bolt holes was added to provide a lifting point and to restrain shrinkage.

In the following paragraphs, the shock tube is introduced, followed by a more detailed description of the component tests, which are summarised in Table 3.

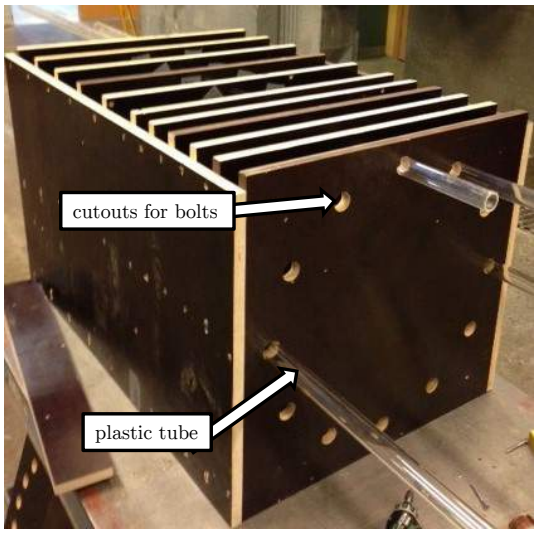

Fig. 2: Wooden mould used to cast slabs.

3.1. Shock tube description

Fig. 3 shows a sketch of the shock tube, with the driver section on the left followed by the driven section in the middle, constituting most of the length of the shock tube. Two pressure sensors (1 and 2) are mounted on the right end, close to where the slabs are clamped. The expansion tank then follows, into which the pressure is relieved if the test specimen fails. Windows are mounted on both sides of the tank, enabling two Phantom v1610 high-speed cameras

Table 3: Data from calibration tests and shock tube experiments on concrete slabs.

	Initial conditions					Experimental results				Figures	
Test ID	P_d [kPa]	ℓ_d [m]	D_t [days]	T_0 [°C]	P_0 [kPa]	P_{peak} [kPa]	v_s [m/s]	i_e^+ [kPa·ms]	t^+ [ms]	$P(t)$ [-]	Photo [-]
M-07	3990	0.27	-	21.8	101	733	581 (-)	8081	51	5(a)	4(a)
M-11	3812	0.77	-	23.6	100	1105	639 (-)	16613	74	5(b)	4(a)
M-16	7766	0.77	-	23.2	100	1623	704 (-)	30149	79	5(c)	4(a)
M-39	7706	2.02	-	21.3	100	3928	730 (-)	59244	89	5(d)	4(a)
C45-07	3948	0.27	32	22.2	98	717	581 (610)	6063	32	5(a)	6(a)
C45-12	4069	0.77	32	24.9	99	1161	654 (658)	15535	56	5(b)	6(b)
C45-17	7620	0.77	91	25.7	100	1712	714 (719)	25415	40	5(c)	6(c)
C45-29	7972	2.02	39	26.0	102	2929	- (769)	26423	18	5(d)	6(d)
C20-11	3940	0.77	49	21.1	103	1145	641 (641)	25940	83	8(a)	9(a)
C20-16	7540	0.77	50	23.6	103	1603	694 (690)	30548	57	8(b)	9(b)
R20-12	4052	0.77	50	21.0	103	1180	641 (637)	25558	77	8(c)	9(c)
R20-17	7375	0.77	50	23.5	103	1688	709 (704)	29255	57	8(d)	9(d)
C20-14	7291	0.77	372	20.6	101	1441	707 (701)	25218	45	11(a)	-
R20-15	7873	0.77	372	20.7	101	1558	703 (698)	25087	44	11(b)	-

to capture the events at a specified frame rate (24 000 frames per second in this study). A detailed description of the shock tube can be found in the work by Aune et al. [8].

The driver and driven sections are separated by diaphragms in the firing section. Here, a pressure difference between the pressurised driver section at (absolute) pressure P_d and the driven section (at atmospheric pressure P_0) is built up in a stepwise manner by multiple intermediate chambers, separated by a specified number of diaphragms. The diaphragm(s) separating each pressure chamber in the firing section is able to withstand a certain pressure gradient $\Delta P < P_d - P_0$. To initiate the shock wave, the intermediate chamber closest to the driver section is rapidly vented to atmospheric pressure, thereby making the pressure gradient over the diaphragm larger than ΔP, thus puncturing the diaphragm. Now, the remaining diaphragms rupture in turn, and the shock wave propagates down the driven section.

A massive steel plate with 10 pressure sensors (labelled 3 to 12 and shown in Fig. 4(a)) was used to measure the arrival times of the shock wave at different locations across the cross-section of the shock tube. The measurements indicated that the arriving shock wave is plane. Pressure sensors 1 and 2 in Fig. 3, flush mounted with the internal wall of the shock tube, registered the pressure close to the slab during each test.

The firing pressure P_d and the length ℓ_d of the driver section (data presented in Table 3) determine the load curve at the test component. It is not a viable solution to mount pressure sensors on an actual test specimen to measure the load; thus, for all combinations of driver length and firing pressure used for the concrete slabs, equivalent tests were performed on the massive steel plate (see Fig. 4(a)) equipped with pressure sensors 3 to 12. The pressure-time histories from sensor 3 in these tests can be observed as solid black lines in Figs. 5 and 8. Data from sensors 1 and 2 in the massive steel plate tests match the data from the corresponding sensors in the concrete tests well in the initial loading phase and for the peak overpressure. This result means that the data from sensor 3 in the massive steel plate tests will provide a good approximation to the load that the concrete slabs experience as long as the deformations in

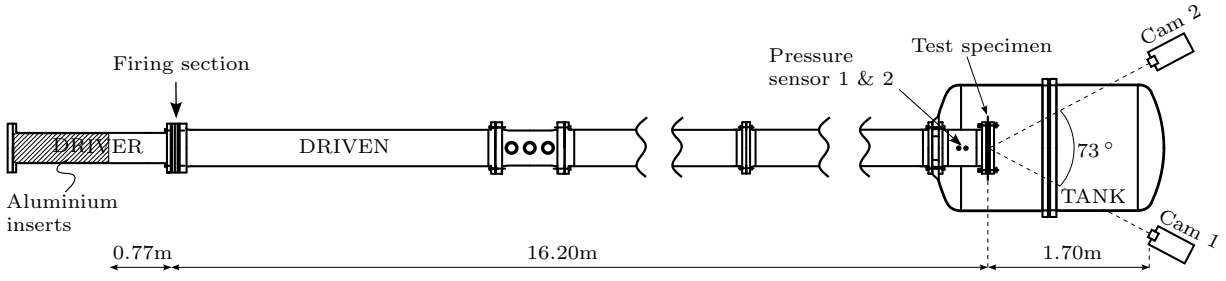

Fig. 3: Schematic view of the shock tube. The volume in the driver can be adjusted by inserting/removing aluminium inserts which alter the length ℓ_d of the driver section (0.77 m in this figure), where a larger volume typically results in a larger impulse, positive phase duration and peak overpressure.

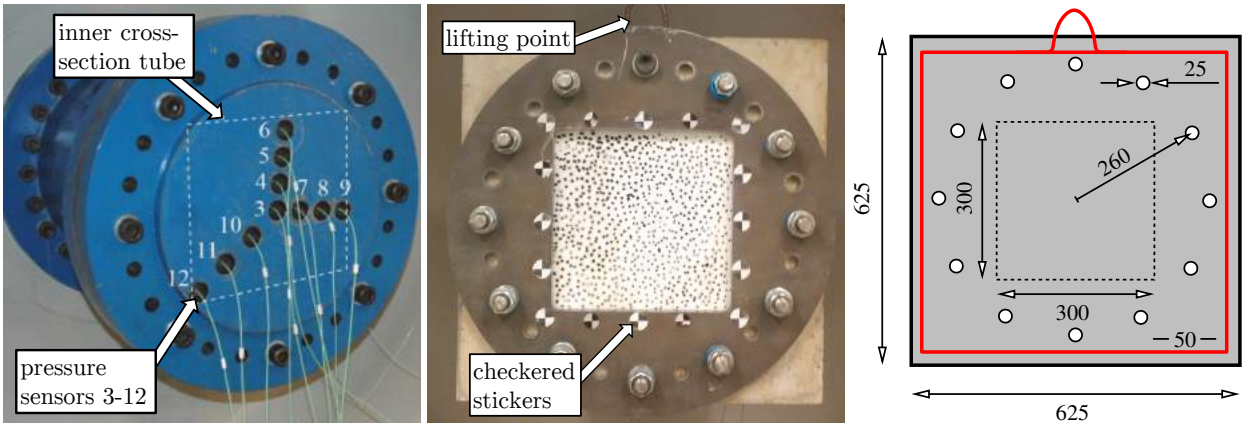

(a) Massive plate with pressure sensors [8] (b) Clamped concrete plate (c) Sketch of concrete slabs in mm

Fig. 4: On the left, (a) is the end section of the shock tube with the massive steel plate with pressure sensors, along with dashed lines showing the inner profile of the shock tube. The centre picture (b) shows a concrete slab (with speckle pattern for 3D-DIC measurements) mounted to the shock tube, while a sketch of the concrete slabs (including the reinforcement for the lifting point) is shown on the right (c).

the concrete slabs are small. A 25 mm thick metal plate is used to clamp the concrete slabs, as depicted in Fig. 4(b). A sketch of the geometry of the slabs is shown in Fig. 4(c). For the C45/55 tests, a steel clamping plate was used, while for the C20/25 tests, either an aluminium plate or a steel plate was used to check whether the clamping plate material exerted any influence on the results.

In Table 3, the slabs are identified by the material (C45 or C20 for short, and R20 for reinforced C20/25 slabs) and by the peak pressure P_{peak} as logged by sensor 2[1], meaning that the C45/55 slab exposed to approximately 0.7 MPa (700 kPa) load is named C45-07 and so on. For the calibration tests using a massive steel plate, an "M" is used rather than "B" or "R", and the centre pressure sensor is used to identify the pressure. The days after casting D_t, temperature T_0 and ambient pressure P_0 are the remaining initial conditions in Table 3. The included experimental data are the peak pressure P_{peak} and the positive specific impulse i_e^+. The duration t^+ of the positive specific impulse is given in ms. The shock wave velocity v_s as calculated based on data from sensors 1 and 2 is also presented. An alternate value based on data from two other sensors closer to the driver section is presented in parentheses. Finally, references to figures showing the pressure-time history $P(t)$ and photographs of the specimens are provided in the last two columns.

3.2. C45/55 series

The target load for the first slab was a 700 kPa overpressure, based on a draft edition of the Norwegian Public Roads Administration's Handbook 185 regarding bridge design [49]. This has since been replaced by the guidelines in N400 [50], which does not provide any specific design overpressure but requires that an assessment is made for each specific project. Generally, a blast load has large variations in peak pressure and duration depending on a large variety of parameters, making it somewhat difficult to standardise compared with other, more common, loads. Nevertheless, 700 kPa [49] was chosen as a basis for further testing as this load is well within the capabilities of the shock tube [8].

The nuts securing the steel clamping plate were tightened very firmly for all the C45/55 slabs, using a large wrench producing a strong torque that was unfortunately not measured. Compared with the torque measured to 140 Nm in subsequent tests, the torque used for the C45/55 slabs is estimated to be higher. Some small but noticeable cracks appeared close to the bolt holes in the C45/55 slabs after tightening the nuts.

As indicated by the grey curve in Fig. 5(a), the first target load of 700 kPa was achieved. For this load, only minor surface cracks were observed on the slab, and the cracks are accentuated by red lines in Fig. 6(a). It was then decided to increase the load by increasing the length ℓ_d from 0.27 m to 0.77 m (and hence the volume) of the driver of the shock tube. Now, the peak overpressure as measured by sensor 2 was approximately 1200 kPa, and some secondary reflections can be observed in the pressure-time recordings in Fig. 5(b). This load produced more noticeable surface cracks, as is evident from Fig. 6(b) without any highlighting.

[1] When the peak pressures were similar, the closest unique integer was chosen.

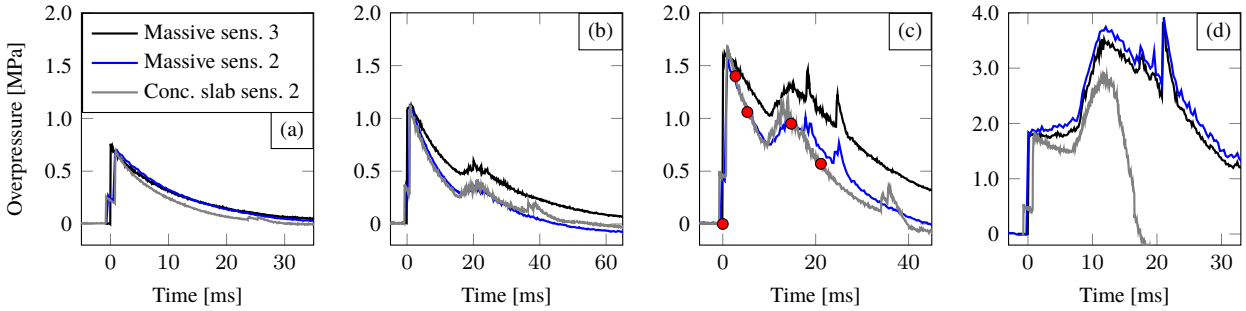

Fig. 5: Pressure-time histories from sensor 2 (sensor 1 in (d)) in shock tube tests of C45/55 concrete slabs (grey curves): (a) C45-07, (b) C45-12, (c) C45-17 and (d) C45-29. Pressure-time data from equivalent tests on a massive steel plate with pressure sensors are shown in black (sensor 3 at the plate) and in blue (sensor 2 close to the plate). The red dots in (c) correspond to the still frames in Fig. 7.

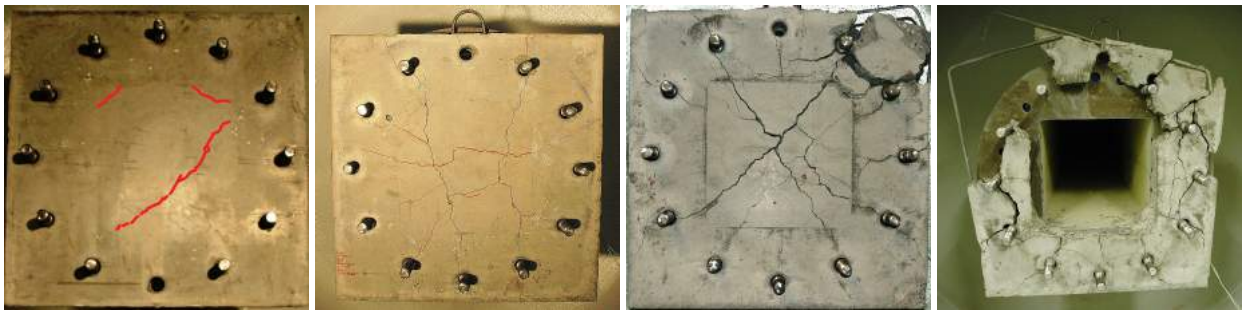

(a) C45-07 (b) C45-12 (c) C45-17 (d) C45-29

Fig. 6: The four C45/55 concrete slabs tested in the shock tube with increasing pressure from left to right. The side shown is opposite to the side where the shock wave arrives.

From the high-speed footage it was possible to identify a few small fragments detaching from the slab. The cracks did not appear to extend through the slab, thereby retaining some structural integrity. FSI effects are typically influential when deformations are large [14, 51]; thus, due to the small deformations and the absence of through-thickness cracks in the slabs, it is concluded that any FSI effects are negligible for C45-07 and C45-12. The pressure-time histories from the concrete tests (grey curves in Fig. 5) are very similar to the pressure recordings from the same sensor (sensor 2, blue curves) in the calibration tests on the instrumented massive steel plate. This result indicates that the pressure from sensor 3 (black curves) is a valid representation of the pressure at the concrete slab.

By further increasing the pressure to approximately 1700 kPa, larger pressure reflections were observed, as shown in Fig. 5(c). The slab now suffered through-thickness cracks (see Fig. 6(c)), which were observed from the video recorded by the high-speed camera. In the video, air (made visible by dust particles) is clearly escaping through the concrete, and fragments come off the slab as depicted in Fig. 7. Here, the yellow arrows in the middle picture show the areas through which the air was able to penetrate first. These areas are close to the boundary of the load area, and in the later images, the through-thickness cracks extend towards the centre of the slab. It appears that FSI effects for this case amount to the leakage of pressure through the plate. This alters the pressure-time history only to a small degree compared with the massive plate tests since the volume passing through a narrow slit is very limited. In Fig. 5, the differences between the grey (concrete test) and blue (calibration test) curves are small in the early stages of the test, while some deviations occur when through-thickness cracks appear (after the second peak, cf. Fig. 7). The slightly different firing pressures P_d between the tests also affect the pressure-time histories. The lowest pressure causing through-thickness cracks is estimated to be between 1161 kPa and 1712 kPa (see Table 3).

The largest pressure in this test series caused a complete collapse of the concrete slab. Fig. 6(d) shows the remnants of the C45-29 slab, while the part not shown was largely pulverised. From Fig. 5(d), the pressure drops rapidly after attaining the peak value since the concrete ruptures completely and the air is allowed to pass more or less freely into

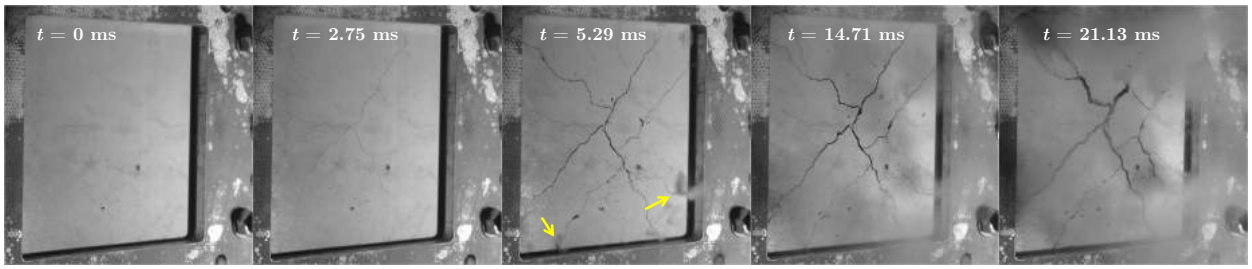

Fig. 7: High-speed footage of C45-17, where the first image from the left shows the undamaged slab just before the shock wave arrives. After 2.75 ms, just after the initial peak, a few surface cracks have appeared, while at 5.29 ms, through-thickness cracks are present, as indicated by dust and air escaping through the slab (look near the yellow arrows). Having passed the secondary peak in Fig. 5(c), more fragments come off the slab (at 14.71 ms). In the final image, taken at 21.13 ms, the cracks are wide open and dust is starting to obscure the view.

the expansion tank. This fourth C45/55 slab completes a good test series, ranging from minor surface cracks for the lowest load to complete collapse for the highest load. For all slabs, the cracks arising in the load area typically connect with the bolt holes.

3.3. C20/25 series concrete

For the C20/25 tests, the two middle pressure levels from the C45/55 series were chosen because they produced surface cracking and through-thickness cracks. These two loads were each applied to the two plain C20/25 concrete slabs and to the two C20/25 concrete slabs with steel reinforcement (labelled R20 in Table 3). Pressure-time histories from these four tests are plotted in Fig. 8. When tightening the nuts for the clamping plate, care was taken to create a snug and tight fit without producing any cracks, as opposed to the C45/55 slabs, which suffered some small cracks in this phase. Two additional tests (one without and one with reinforcement) were conducted using a steel clamping plate rather than aluminium, and the higher of the two loads (approximately 1.6 MPa overpressure at the concrete slabs).

In the time between the C45/55 series tests and the C20/25 tests, the expansion tank on the shock tube was equipped with a new window on the opposite side of the existing one, which enables the use of a second high-speed camera (see Fig. 3). With two cameras, it is possible to use a 3D digital image correlation (3D-DIC) technique to measure the deformations in the slabs. In this study, the finite element based DIC code eCorr [52] was used for all DIC measurements.

The slabs were consequently painted for 3D-DIC use, and this speckled paint pattern is shown in Fig. 4(b) and Fig. 9. The pattern had a size distribution in the range of 2-4 mm, equivalent to approximately 3-7 pixels, where the speckle size was based on minimising the effect of aliasing in the DIC code [8]. Three different calibration setups were used in the computation of the deformations, with very little variation between them (tenths of millimetres). This result confirmed that the DIC procedure is consistent and well suited for this application.

When the pressure is released, the shock tube recoils in a rigid body motion. To measure this movement, checkered stickers were glued to the clamping plate to serve as reference points (see Fig. 4(b)). From the DIC, this movement

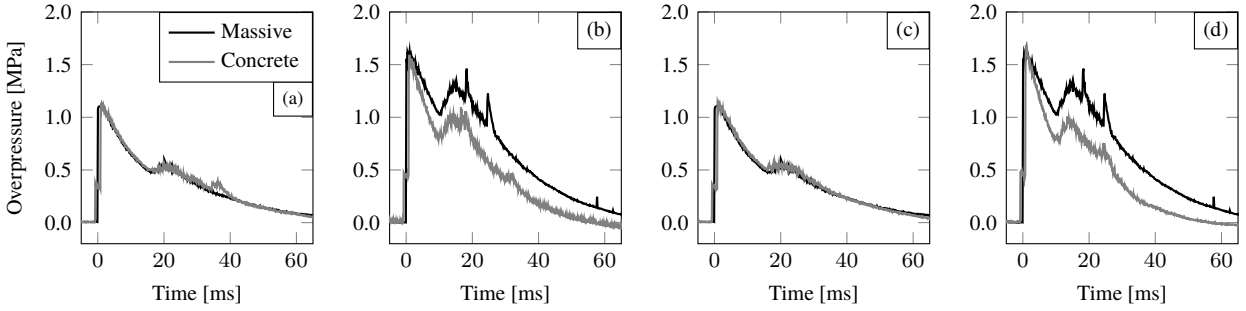

Fig. 8: Pressure-time histories (grey) from sensor 2 in shock tube tests of C20/25 concrete slabs: (a) C20-11, (b) C20-16, (c) R20-12 and (d) R20-17. The results from tests performed on a massive steel plate with pressure sensors are shown as solid black lines.

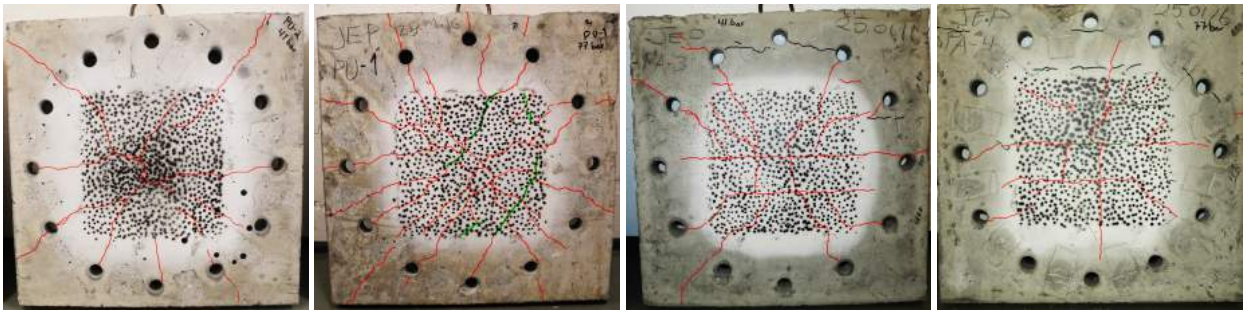

(a) C20-11 (b) C20-16 (c) R20-12 (d) R20-17

Fig. 9: The four C20/25 concrete slabs tested in the shock tube. The side shown is opposite to the side where the shock wave arrives. Pre-existing cracks are highlighted with green, while cracks arising from the shock tube tests are red.

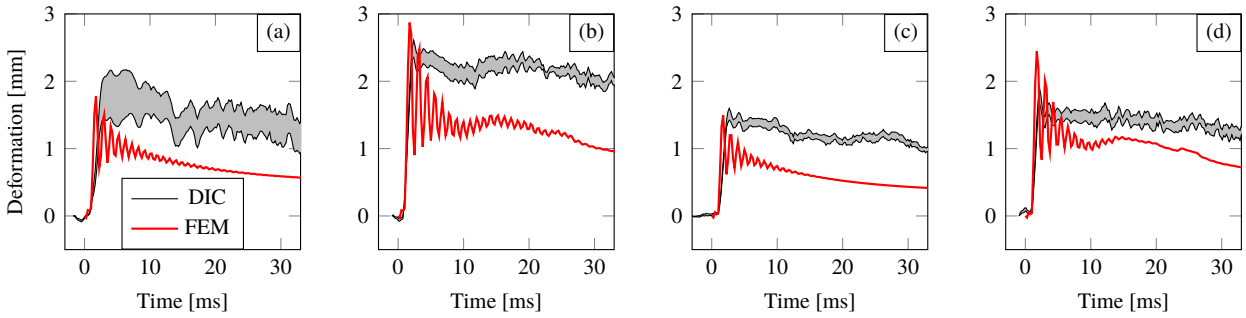

Fig. 10: Mid-point deflection from DIC (grey) in shock tube tests of C20/25 concrete slabs: (a) C20-11, (b) C20-16, (c) R20-12 and (d) R20-17, while the red lines show the results achieved by FEM.

was registered and subtracted from the measured displacement of the plate to obtain the actual deformation of the plate. The movement was measured at four points across the clamping, and the mean of these measurements was used to correct the deformations measured in the concrete slab. The results are shown in Fig. 10, where the out-of-plane displacement bands of the four nodes of the centre element from the DIC analysis are plotted. The lower curve is the smallest displacement of the four nodes and the higher is the larger, and the other two lie in the hatched grey area in between. The red lines indicate the mid-point deflection obtained by the finite element method (FEM) described in Section 4.

The most notable difference between the C20/25 and the C45/55 slabs is the absence of open through-thickness cracks in the former (see Fig. 9), as shown in Fig. 6(c) for comparable loading. As C20/25 is a weaker mix, larger and more prominent cracks were expected. With the loads being of similar magnitude, the discrepancy is most likely caused by other parameters. A lower torque was used for the C20/25 series, resulting in smaller and/or fewer micro cracks appearing during bolt tension, lower stiffness of the system, and lower initial stresses in the concrete. The effect of the bolt force is therefore investigated numerically in Section 4.3. In addition, an aluminium clamping plate was used rather than steel. When the stiffness of the test object (concrete slab in this case) is close to the stiffness of the frame clamping it, deformations are likely to also occur in the clamping plate.

In all the C20/25 slabs, surface cracks were dominant, and the reinforcement reduced the deformation (clearly observed in Fig. 10) and directed the cracks along the reinforcement grid, as also observed by Tu and Lu [46]. For this problem, it is demonstrated that potential FSI effects are limited to leakage either via through-thickness cracks or small gaps between the clamping and the test slab, but these effects are small and difficult to isolate. No obvious through-thickness cracks were observed, although the concrete, with and without reinforcement, appeared to be on the brink of giving in. The lowest pressure causing through-thickness cracks is estimated to be slightly above 1688 kPa.

Finally, the two tests with the highest load were repeated with one difference: the aluminium clamping plate was replaced by a steel plate. The higher of the two loads was chosen, and one slab without reinforcement and one with

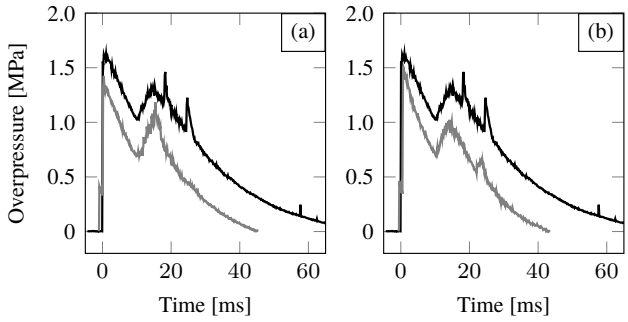

Fig. 11: Pressure-time histories from sensor 2 (grey lines) in shock tube tests of C20/25 concrete slabs with steel clamping plate, where (a) is C20-14 and (b) is R20-15, along with tests performed on a massive steel plate with pressure sensors (black lines).

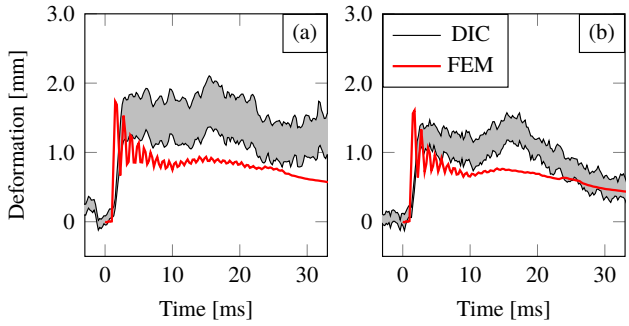

Fig. 12: Mid-point deflection histories from DIC (grey) and FEM (red) of shock tube tests of C20/25 concrete slabs: (a) C20-14 and (b) R20-15.

reinforcement were tested, called C20-14 and R20-15, respectively, in Table 3. Pressure-time histories are shown in Fig. 11, and DIC measurements are shown in Fig. 12. Although the out-of-plane deformation is above 2 mm in Fig. 10(b), it is below 2 mm in Fig. 12(a). This result is partly due to the steel clamping frame and partly due to a slightly lower pressure load. Due to a worn out O-ring, the desired firing pressure P_d was not fully attained for C20-14, causing a gap between the peaks of the grey and black curves in Fig. 11(a). The O-ring was replaced and worked well for R20-15. The levels of deformation, both relative and absolute, are in accordance with expectations. In addition, the tightening torque T_t was now measured to 140 Nm using a torque wrench. By using a commonly assumed nut factor K of 0.2 [53], the pretension force P_{pre} in the bolts is estimated to approximately 30 kN by the following relation [54]:

$$T_t = K \cdot d_b \cdot P_{\mathrm{pre}} \tag{1}$$

in which d_b is the bolt diameter.

4. Numerical simulations

Finite element simulations of the component tests are conducted using the explicit version of the solver LS-DYNA [43]. The main goals of the simulations are to investigate the effects of various parameters qualitatively during blast loading of concrete slabs and to assess the level of quantitative accuracy obtainable by using some of the techniques available in the code.

4.1. Setup of simulations

All simulations are purely Lagrangian, and the blast load is applied as a uniform pressure across the load area measuring 300 mm × 300 mm (see Fig. 4(c)). Pressure-time histories are taken from the massive-plate experiments. Fig. 13 shows a rendering of the numerical setup, which consists of four major parts: the shock tube flange, the

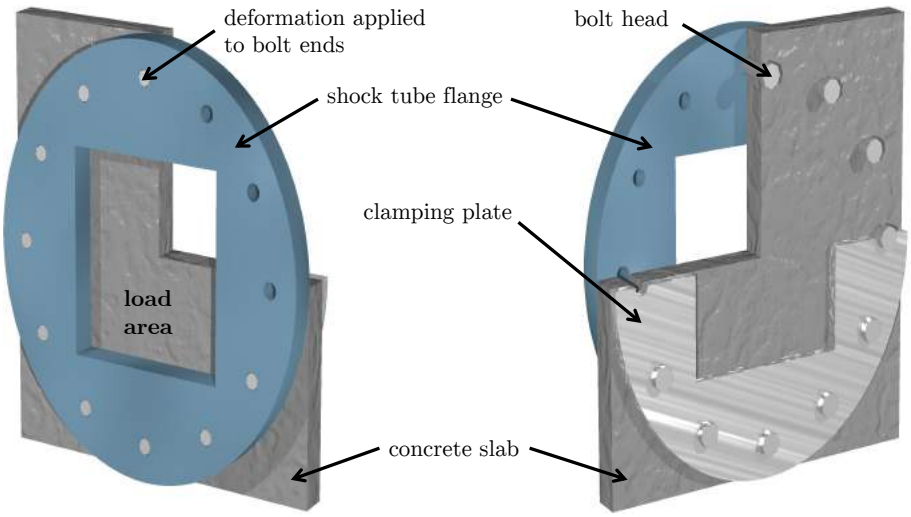

Fig. 13: Rendering of the numerical setup for the simulations, showing the front where the shock wave arrives (left) and the back which was filmed by the high-speed cameras in the experiments (right). The clamping plate and the concrete slab have been cut and three of the bolts have been removed to show all the parts more clearly.

concrete slab, the clamping plate, and the bolts. The concrete slab is placed in contact with the shock tube flange and the clamping plate on the outside of the slab as in the experiments.

Twelve bolts then ensure that all parts are clamped together. All four parts are meshed with eight-node linear brick elements with reduced integration. Simulations using different element sizes showed that a fair compromise between speed and accuracy was obtained at an element size of approximately 10 mm (meaning five elements across the thickness). If more detailed crack patterns are of interest, then a finer mesh should be used. No extra damping is included in the model. When relevant, steel reinforcement bars are included as a fifth part using two-node beam elements with six degrees of freedom per node as this is a common and tested approach for including reinforcement in concrete [34, 55]. The beam elements are then superimposed with the solid mesh using the "Constrained Lagrange in solid" keyword [43], which assumes a perfect bond. Given a sufficiently fine discretisation, using solid elements also for the reinforcement bars would give more accurate results for large deformations. In addition, solid elements would enable modelling of the potential debonding between the concrete and the reinforcement. However, because the plastic deformation of the steel grid was minor (at most), and because no significant slip between the reinforcement and the concrete was noted in the experiments, the beam element approach should yield sufficient accuracy while keeping the CPU cost a reasonable level.

The surface nodes of the shock tube flange facing away from the concrete slab are restrained in all spatial directions, simulating the fixed connection to the rig. Between all four major parts, a penalty-based surface-to-surface contact formulation is used with a friction coefficient of $\mu = 0.4$ between each other. To emulate the tension force in the bolts, a small displacement is applied to the end of each bolt (see Fig. 13), thereby causing the bolt head to restrain the clamping plate. The magnitude of this displacement was chosen such that the force in the bolt conformed with the estimate from Eq. (1), which was approximately 30 kN.

While all the different parts (end of shock tube, prestressed bolts, and clamping plate) may seem excessive at a glance, they are quite important. A first attempt was made to model the concrete slab alone, using only nodal constraints [56]. The nodes in the bolt holes were constrained from any radial motion, while the nodes in contact with the shock tube and the clamping plate were restrained from out-of-plane movement. This led to an overly constrained system only reproducing parts of the damage pattern and with much lower damage magnitudes compared with simulations using contact boundary conditions. Fig. 14 shows a fringe plot of the scaled damage parameter δ (see Section 4.2) in the slabs at the end of the simulation. This shows that an accurate representation of the boundary conditions is crucial for good results. When using only nodal constraints, the simulation time was 11 minutes on a single CPU. When including all the parts, the simulation time increased to about 75 minutes. Further, the hourglass

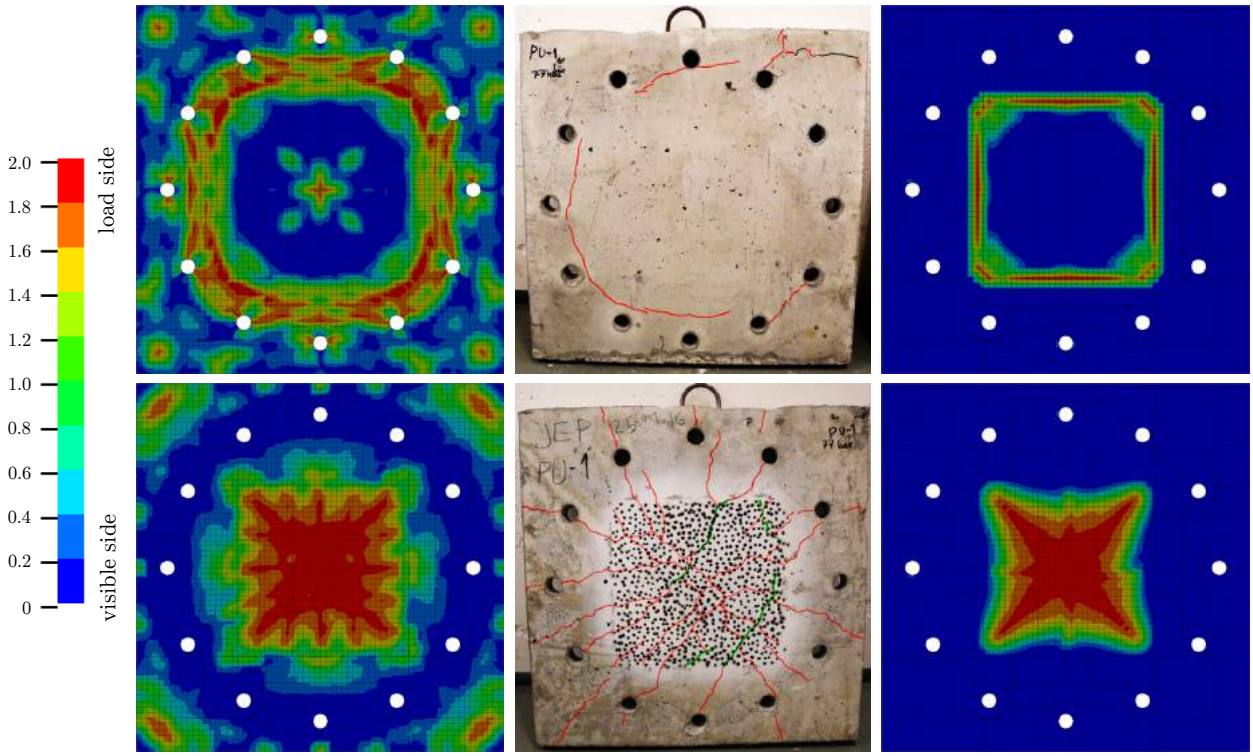

Fig. 14: Results from the numerical investigation of the boundary conditions, showing a fringe plot of the scaled damage parameter δ in the slabs at the end of the simulation.

technique used was quite critical to the outcome, with stiffness-based hourglass models outperforming the viscous ones and therefore being preferred in simulations involving fast transient dynamics [57, 58]. When changing the hourglass technique from the default (viscous) to the stiffness based with exact volume integration, the hourglass energy dropped from above 30% to approximately 3%.

The base case for the numerical studies is an unreinforced C20/25 concrete slab with a steel clamping frame exposed to a peak pressure load of approximately 1200 kPa (the black curve in Fig. 5(b)). Then, alterations are made one at a time to this numerical setup, and the differences in results caused by these alterations are assessed to determine what influence each parameter exerts. The parameters to change, one at a time, are the following (initial values given):

- Doubling and halving of the unconfined compressive strength $f_{cc} = 39.6$ MPa
- Doubling and halving of the tensile strength $f_t = 3.5$ MPa
- Doubling and halving of the tensile force $P_{\text{pre}} = 30$ kN in the bolts
- Doubling and halving of the coefficient of friction $\mu = 0.4$

After testing the effects of changing these parameters, an attempt is made to recreate some of the component tests for comparison with the experimental results. The C20-16 test (cf. Table 3) is used as a base case, while some distinct changes are made to the model, and the changes are following:

- Decreasing the load (C20-11)
- Adding reinforcement (R20-17)
- Changing the concrete from C20/25 to C45/55 (C45-17)

- Substituting the aluminium in the clamping plate with steel (C20-14)

The test IDs given in parentheses in the list above match the corresponding tests from Table 3.

4.2. Material models

All metal parts except for the reinforcement are modelled as isotropic and linear elastic materials with the material parameters given in Table 4. The shock tube flange and the bolts are always modelled as steel, while the clamping plate can be steel or aluminium.

A bilinear material model was used for the reinforcement, with a yield stress of 794 MPa and a tangent modulus of 1039 MPa. The Young's modulus used was 210 GPa, and the Poisson ratio was 0.33. For plasticity, the von Mises yield criterion was applied with the associated flow rule. Because the plastic deformations of the steel grid were considered to be minor in this problem, no strain rate sensitivity is accounted for in the constitutive relation for the reinforcement, and no failure criterion is used.

The concrete is represented by the K&C model [44, 45], a widely used model [27, 46, 56, 59] requiring only one material parameter (aside from the Poisson ratio ν), which is the unconfined compression strength f_{cc}. The other parameters (including Young's modulus) for the model are then generated based on this value. The generated values are then written to an output file from which it is possible to copy the data into a new input file. If one has additional values from laboratory testing, for instance the tensile strength f_t like here, this can be changed in the new input. The concrete material parameters used are presented in Table 2, and the Poisson ratio is taken as $\nu = 0.2$. The damage parameter δ [43] – which is between 0 and 1 in the hardening phase and between 1 and 2 in the softening phase – is used in contour plots later. A more detailed presentation of the concrete model can be found elsewhere [44, 45].

Table 4: Elastic properties for metals used in simulations.

Material	E [MPa]	ρ [kg/m^3]	ν [-]
Steel	210 000	7 800	0.33
Aluminium	70 000	2 700	0.33

4.3. Numerical results

The overall results of the parameter studies doubling and halving various parameters are shown in Fig. 15 as fringe plots of the scaled damage parameter δ [43]. The base case is in the centre (part (e)), with doubling and halving four different parameters surrounding the base case for easier comparison. Changing f_{cc} (parts (a) and (b)) does not affect the result to any significant extent, and the friction μ also has a minor effect (parts (h) and (i)). The pretension in the bolts has a major effect, where doubling the force (part (d)) causes a large increase in the damaged area, both during the pretension phase and during the pressure load phase. Halving the force makes the slab less constrained and does not damage the slab as much during clamping, as shown in the lower left of Fig. 15 (part (g)). Tighter bolts make the slab resemble a fully clamped plate, whereas looser bolts tend to make the slab behave more like a simply supported plate. Reality is somewhere between these two extremes. Making an accurate estimate of the experimental P_{pre} is not easy, which in turn makes accurate numerical predictions difficult to obtain. The tensile strength f_t had the largest effect by far, as halving the value caused a severely damaged slab (part (c)). Conversely, doubling the value reduced the extent of the damage considerably as illustrated in part (f) of Fig. 15. This result is consitent with expectations because bending is the main mode of deformation.

Turning to Fig. 16, the results are generally in agreement with expectations – the base case C20-16 (centre column) suffers more damage than the C20-11 case (left column) due to the magnitude of the load. Because f_{cc} did not greatly affect the results in Fig. 15, it is reasonable to assume that the difference between C20-16 and C45-17 in Fig. 16 is mainly due to the increased f_t. The only difference between C20-16 and C20-14 in the numerical model is the clamping plate, which is aluminium in the former and steel in the latter. This apparently caused a marked damage reduction due to the higher Young's modulus of steel. Changing the clamping plate's material to steel yields a lower out-of-plane deformation and lower strain (compare Fig. 10(b) and (d) with Fig. 12). This result means that the clamping plate is important to the system stiffness and should be taken into consideration for future tests. When the test component has a stiffness similar to the clamping plate, deformations also occur in the clamping plate. The out-of-plane deformation of

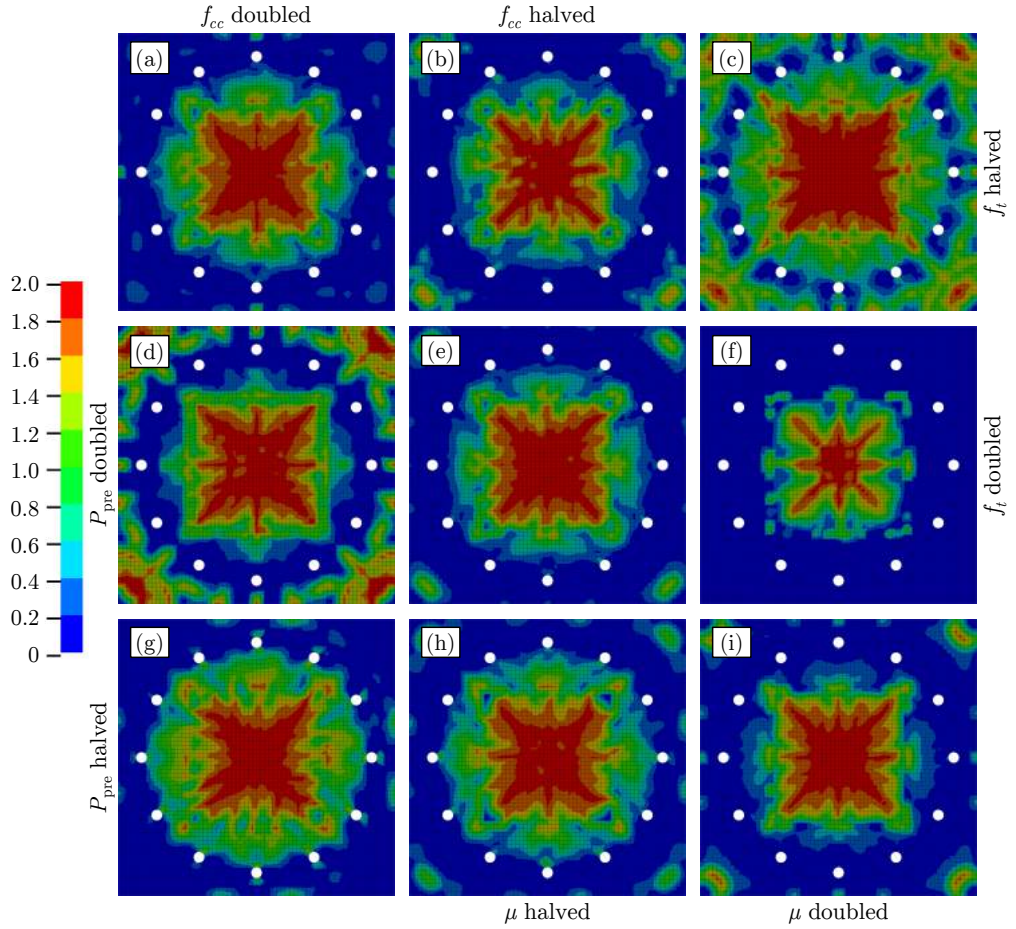

Fig. 15: The results from the parameter studies, showing fringe plots of the damage parameter δ. The base case is in the centre, while the eight other parts represent a doubling or halving of each parameter.

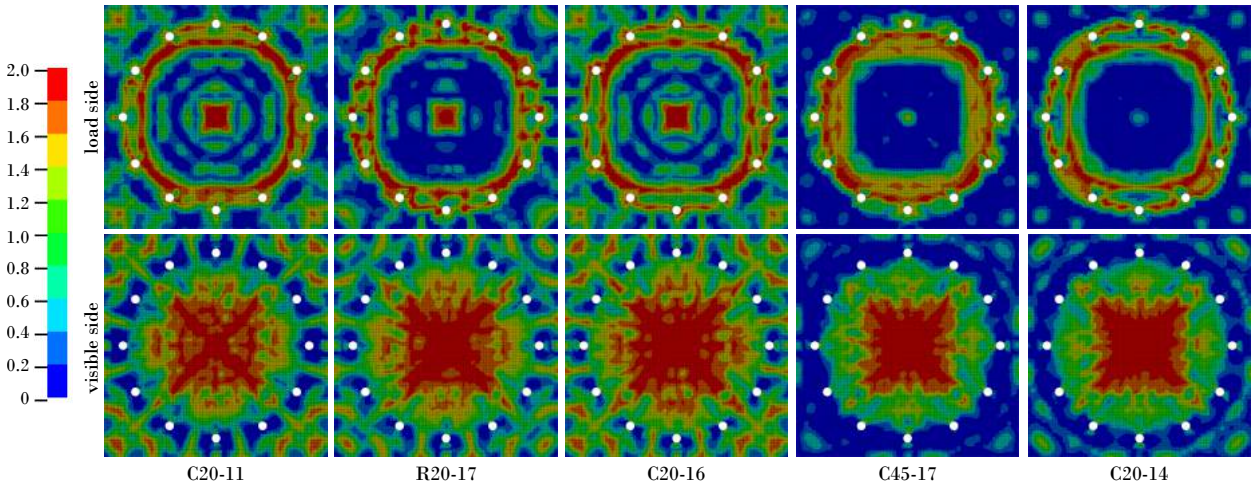

Fig. 16: The results from the numerical recreations of the component tests, showing fringe plots of the damage parameter δ.

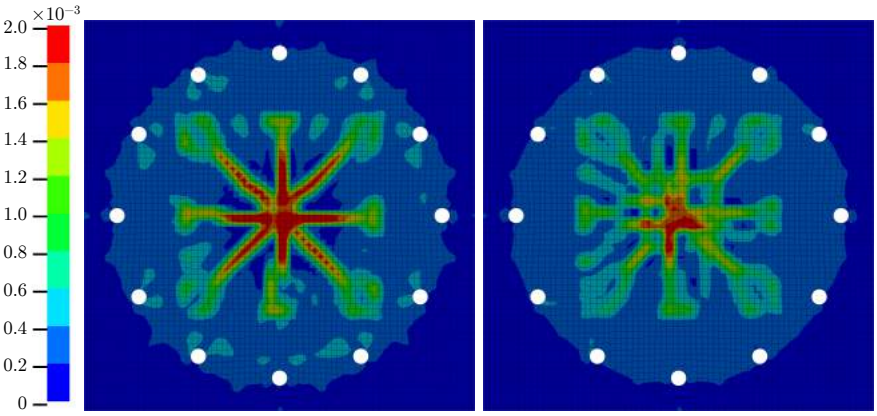

Fig. 17: Green strain after 1.5 ms simulation time in the C20-11 test (left) vs. the R20-12 test (right).

the midpoint can be observed as solid red lines in Fig. 10, where they are compared with the experimentally obtained 3D-DIC measurements. Qualitatively, the agreement is consistent, and the second "hump" in deformation for the higher load is captured. The quantitative values are not exact, but still quite decent as these values were obtained without any tweaking of the numerical input.

Finally, the difference between C20-16 and R20-17 in the numerical model is caused by the reinforcement in the latter. As shown in Fig. 16, the extent of the damage is reduced when reinforcement is included. Additionally, the strains are reduced in magnitude and more directed along the reinforcement. This is not immediately apparent from Fig. 16, but it can be observed in Fig. 17 which shows the effective Green strain in a plain concrete slab (left) and a reinforced concrete slab (right) after a simulations time of 1.5 ms.

5. Discussion

5.1. Material tests

The difference between cube compression (confined) and cylinder compression (unconfined) was consitent with expectations. Tensile splitting tests provided an estimate of the tensile strength close to the theoretical/empirical prediction by Eurocode 2 [48]. For C45/55, the range from minimum to maximum measured f_t was 3.8 MPa to 4.4 MPa, while the range for C20/25 was 3.0 MPa to 4.1 MPa. Since this parameter is highly influential on the numerical results, the variation in this parameter should be accounted for since an average value may not accurately represent the material.

Twenty cube compression tests on the C20/25 concrete showed that the scatter is fairly low. If smaller cubes were produced, either by casting in a smaller mould or by cutting larger samples, then they would surely produce a larger scatter than the larger cubes as the variation from one point in the concrete to the next can be quite large due to the aggregate, air content, degree of hydration and various other parameters [60–62]. The C20/25 concrete was also tested at various stages of curing. Up to and including 49 days of curing, this concrete behaved as expected, while the long-term cube compression strength (84 days) was somewhat higher compared with the predictions by EC 2 [48]. This is due to the cubes being submerged in water for curing until the day of testing. Hence, the 28-day strength of each concrete is used as the basis for the strength of the slabs.

Conventional quasi-static tension tests with an extensometer provided an engineering stress-strain curve valid up to necking for the steel reinforcement, which had a fairly high yield stress (766.4 MPa). The true fracture strain as measured by an optical microscope was 0.880, indicating a ductile material, at least compared with the concrete.

5.2. Component tests

The SIMLab Shock Tube facility [8] is an excellent tool for emulating blast loads against plated structures. It produces consistent loads, and together with high-speed cameras and 3D digital image correlation, very good experimental data sets are obtainable. When testing concrete, there are a few caveats. The torque used to tighten the

nuts for the clamping plate is important and should be measured for consistency and to avoid cracks appearing in the concrete. Additionally, some seal (e.g. rubber) should be applied around the mouth of the shock tube to avoid potential leakage, which may have been present here. The application of large loads can cause unwanted secondary reflections, altering the shape of the pressure-time curve to something slightly different than what characterises an idealised blast load, as was the case in Fig. 5(d).

A nice set of experiments for C45/55 slabs was produced, ranging from very small surface cracks in Fig. 6(a) to total destruction in Fig. 6(d). The concrete slabs themselves were able to withstand a fair amount of pressure given their relatively low thickness, well above 700 kPa [49]. Preliminary drawings for a submerged floating tunnel suggest a wall thickness up to 1000 mm. Although not directly applicable to an SFT, a plate's flexural rigidity is proportional to the cube of the thickness [63]; thus, 1000 mm thick walls would most likely provide sufficient capacity for pressure loads of magnitude well above those investigated herein. Regardless, scaling of concrete is not straightforward due to aggregate and filler size, strain rate sensitivity and so forth.

The C20/25 slabs suffered less cracking than expected compared with the C45/55 tests, and this may be attributed to the lower torque applied when clamping the slabs. The dynamic increase factor of concrete may also limit this difference [37]. For future studies of this type, one should take care to measure the tightening torque for all tests and ensure that it is consistent. It was also shown that the tensile strength dominates this problem, and the measured tensile strength overlapped in several tensile splitting tests. Images from the high-speed cameras revealed potential leakage between the concrete slab and the shock tube, although this may be dust that was already present. Adding reinforcement to the C20/25 slabs reduced the deformation as expected and directed the cracks along the lines of the reinforcement grid.

The use of 3D digital image correlation was helpful for quantifying the deformations and showed the effect of the reinforcement and of the magnitude of the load. For the C20-14 and R20-15 tests, a laser measured the rigid body motion of the tank end of the shock tube. These laser measurements were compared with point tracking from the DIC, and the results are shown in Fig. 18 (the origin of the two measurements have been juxtaposed and do not coincide with the origin in other figures). As shown, the point tracking matches the laser-based measurements closely, but differ somewhat later in the test. The discrepancy could be due to slight deformations in the clamping plate, which has the point tracking stickers attached to it, or dust obscuring the cameras' field of vision. Additionally, the laser measured the rigid body motion on the outside of the dump tank while the point tracking is measured on the clamping frame.

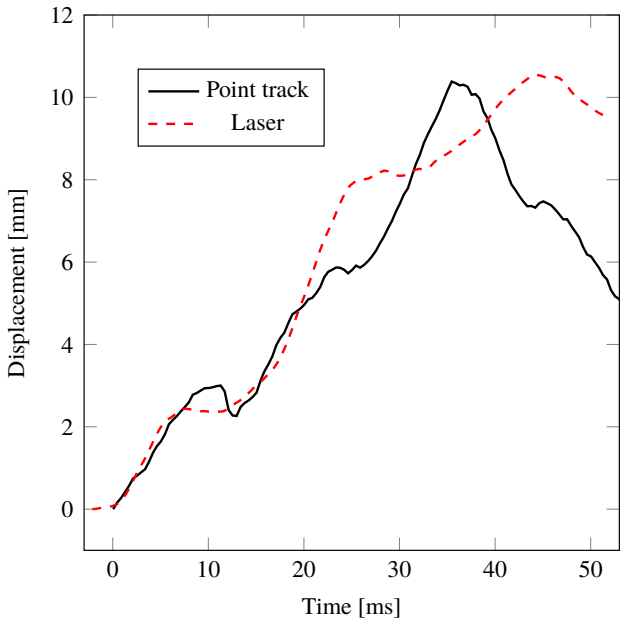

Fig. 18: Point tracking (solid) vs. laser measurements (dashed) for the rigid body motion of the shock tube in the C20-14 test.

Some of the deviation may be related to the eigenoscillations in the longitudinal axis of the tube and their interaction with the wave pattern inside [8]. Regardless, the measurements match well and help validate the DIC procedure. The relative differences between the mid-point deflections of the concrete slabs as calculated by the DIC technique were also consistent with expectations.

Finally, the material in the clamping frame can be influential. Judging from the results herein, the stiffness of the test specimen should be an order of magnitude lower than the clamping plates to limit the deformations to the test specimen. In these cases, the stiffnesses were fairly close, causing the clamping frame, either aluminium or steel, to be part of the tested system, as confirmed by the simulations. A steel clamping frame reduced the out-of-plane deformation obtained by DIC, showing that the aluminium frame caused a more compliant system.

5.3. Numerical simulations

Given the fairly simple setup, the numerical simulations provided decent results. The damage pattern indicated by the scaled damage parameter δ replicates the observations from the experiments in all simulations, except with the simplified boundary conditions using nodal constraints (the right part of Fig. 14). Including the end of the shock tube, the clamping plate and the bolts were important for properly capturing the events. Altering the contact algorithm (penalty-based herein) may affect the simulation results but was beyond the scope of this study. Choosing the correct hourglass technique can be critical to obtaining decent results. Although predicting an exact response (deflection) is difficult, numerical simulations have proven to be a very useful tool in evaluating test setups and eventually structures.

The effects of the parameter alterations were captured qualitatively in the simulations with the suggested model – only standard out-of-the-box techniques were employed. Although the unconfined compressive strength did not greatly affect the simulations, the tensile strength was very influential, as was the bolt force, which can be a difficult test parameter to estimate accurately. Simulations are helpful for assessing which parameters can help reduce cracking for concrete parts exposed to blast loading, even if exact predictions were not obtained here. Qualitatively, the numerical models captured the observed effects, and Fig. 10 shows that the quantitative results are also quite decent.

For more detailed results, e.g. accurate crack patterns, more in-depth models are required. For instance, modelling the conglomerate concrete as a homogeneous entity leaves room for improvement. Accounting for the spatial variation of the strength and/or the effect of the aggregate would be a natural next step, e.g. as suggested in mesoscale models [64, 65]. Since f_t was quite dominant – and there was some scatter between the tests – taking this into account should produce more realistic results. This point is emphasised by Fig. 19, which shows the base case C20-16 in the centre column. In the left column, an identical simulation is run, but the average measured f_t has been exchanged with the lowest, while in the right column, the highest measured f_t has been used.

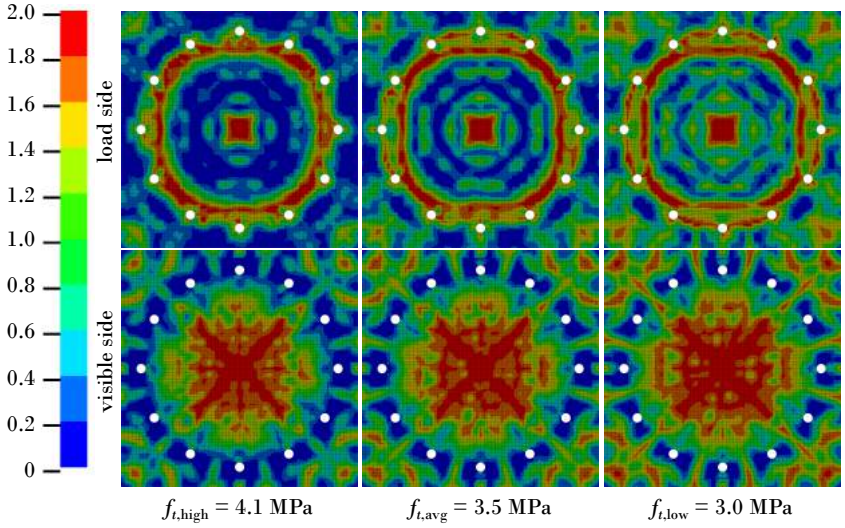

Fig. 19: Simulations using the highest (left column) and lowest (right column) measured values of f_t compared with the average value (centre column). Fringe plot shows the scale damage parameter δ.

6. Concluding remarks

In this paper, the blast performance of concrete slabs has been investigated both experimentally and numerically. The main conclusions from the study are as follows.

- Based on a number of material tests – cube compression, cylinder compression and tensile splitting – the scatter in the experimental results was found to be low despite the inherent heterogeneity of concrete at the macroscopic level.
- The compressive strength of the ordered C45/55 concrete was found to be in accordance with EC 2, while the ordered C20/25 concrete was determined to be closer to a C30/37 concrete, indicating the necessity of a proper material test campaign when working with concrete structures.
- The shock tube used in the component tests produced consistent and blast-like loading conditions, and the applied 3D-DIC technique synchronised with the pressure recordings proved to be a reliable and valuable deformation measurement tool during blast loading.
- By successively increasing the blast load against the C45/55 concrete slabs, it was possible to alter and follow the response from minor surface cracks, to noticeable surface cracks, to through-thickness cracks, and finally to complete collapse. Such data are critical when it comes to validation of e.g. analytical or numerical computations.
- Only two different pressures were applied for the C20/25 concrete plates, but these were tested both with and without steel-bar reinforcement. The boundary conditions were also varied in these tests by changing the clamping frame material.
- Adding steel-bar reinforcement reduced the deformation of the concrete slab as confirmed by the 3D-DIC measurements, and directed the cracks along the reinforcement grid. Furthermore, both the bolt pre-tension and the clamping plate material affected the response of the concrete slab to some extent.
- Based on a numerical parameter study, it was found that changing the unconfined compressive strength and the frictional coefficient had a relatively minor effect on the structural response of the concrete slab, while changing the pre-tension in the bolts and particularly the tensile strength of the concrete had a major influence.
- It was also numerically found that the material in the clamping plate is important to the system stiffness, and that it is of the utmost importance to model the boundary conditions as accurately as possible. Using only nodal constraints is insufficient.
- Both the strains and the damage in the concrete slabs were reduced in the numerical model when steel-bar reinforcement was included.
- The effects of the concrete mix, steel-bar reinforcement, bolt tension and load intensity were all qualitatively captured by the numerical model. The quantitative results were also found to be in reasonable agreement with the experimental results, even though differences were observed. For more detailed simulation results, such as an accurate crack pattern, a more in-depth numerical model than the one used in this study is required.

Acknowledgements

The authors would like to express their gratitude to the E39 Coastal Highway project by the Norwegian Public Roads Administration, which has funded the present work. Parts of this work have also been financed by the Research Council of Norway through the Centre for Advanced Structural Analysis, Project No. 237885 (CASA). Additional thanks to Trond Auestad, Eivind Hillestad, Karoline Osnes and Sondre Rydtun Haug for help with the experimental parts of this work.

References

[1] B. Jakobsen. Design of Submerged Floating Tunnel operating under various conditions. *Procedia Engineering*, 4:71–79, 2010.

[2] *A feasibiliy study – How to cross the wide and deep Sognefjord*. Statens Vegvesen, 2011. http://www.vegvesen.no/_attachment/274047/binary/485789.

[3] A. Fjeld, T.H. Søreide, and S.A. Haugerud. Mulighetsstudie for kryssing av Sognefjorden – Neddykket rørbru. Technical report, Reinertsen AS, Dr. Techn. Olav Olsen, 2013. Document no. 11744-ROO-R-002.

[4] S. Remseth, B.J. Leira, K.M. Okstad, K.M. Mathisen, and T. Haukås. Dynamic response and fluid/structure interaction of submerged floating tunnels. *Computers and Structures*, 72:659–685, 1999.

[5] X. Xiang, M.E. Eidem, J.H. Sekse, and A. Minoretti. Hydrodynamic loads on a sugmerged floating tube bridge induced by a passing ship or two ships in maneuver in calm water. *Proceedings of the ASME 2016 35th International Conference on Ocean, Offshore and Arctic Engineering*, 2016.

[6] Y. Xiang and Y. Yang. Spatial dynamic response of submerged floating tunnel under impact load. *Marine Structures*, 53:20–31, 2017.

[7] *Statens Vegvesen*, Accessed 15.05.2018. http://www.vegvesen.no/Vegprosjekter/ferjefriE39/English.

[8] V. Aune, E. Fagerholt, M. Langseth, and T. Børvik. A shock tube facility to generate blast loading on structures. *International Journal of Protective Structures*, 7:340–366, 2016.

[9] W. Wilkinson, D. Cormie, and M. Arkinstall. Calculation of blast loads for design against terrorism. *Engineering and Computational Mechanics*, 166:132–139, 2013.

[10] C.N. Kingery and G. Bulmash. Airblast parameters from TNT spherical air burst and hemispherical surface burst. Technical report, Aberdeen Proving Ground, MD: Defence Technical Information Center, Ballsitic Research Laboratory, 1984.

[11] A.M. Remennikov. A review of methods for predicting bomb blast effects on buildings. *Journal of Battlefield Technology*, 6:5–10, 2003.

[12] R. Jayasooriya, D.P. Thambiratnam, N.J. Perera, and V. Kosse. Blast and residual capacity analysis of reinforced concrete framed buildings. *Engineering Structures*, 33:3483–3495, 2011.

[13] V. Karlos, G. Solomos, and M. Larcher. Analysis of the blast wave decay coefficient using the Kingery-Bulmash data. *International Journal of Protective Structures*, 7:409–429, 2016.

[14] V. Aune, G. Valsamos, F. Casadei, M. Larcher, M. Langseth, and T. Børvik. Numerical study on the structural response of blast-loaded thin aluminium and steel plates. *International Journal of Impact Engineering*, 99:131–144, 2017.

[15] R. Rajendran and J.M. Lee. Blast loaded plates. *Marine Structures*, 22:99–127, 2009.

[16] M. Foglar and M. Kovar. Conclusions from experimental testing of blast resistance of FRC and RC bridge decks. *International Journal of Impact Engineering*, 59:18–28, 2013.

[17] J. Li, C. Wu, and H. Hao. Investigation of ultra-high performance concrete slab and normal strength concrete slab under contact explosion. *Engineering Structures*, 102:395–408, 2015.

[18] M. Oña, G. Morales-Alonso, F. Gálvez, V. Sánchez-Gálvez, and D. Cendón. Analysis of concrete targets with different kinds of reinforcements subjected to blast loading. *European Physical Journal – Special Topics*, 225:265–282, 2016.

[19] J. Ekström, R. Rempling, and M. Plos. Spalling in concrete subjected to shock wave blast. *Engineering Structures*, 122:72–82, 2016.

[20] A. Schenker, I. Anteby, E. Gal, Y. Kivity, E. Nizri, O. Sadot, R. Michaelis, O. Levintant, and G. Ben-Dor. Full-scale field tests of concrete slabs subjected to blast loads. *International Journal of Impact Engineering*, 35:184–198, 2008.

[21] Z.S. Tabatabaei, J.S. Volz, J. Baird, B.P. Gliha, and D.I. Keener. Experimental and numerical analyses of long carbon fiber reinforced concrete panels exposed to blast loading. *International Journal of Impact Engineering*, 57:70–80, 2013.

[22] C.P. Pantelides, T.T. Garfield, W.D. Richins, T.K. Larson, and J.E. Blakeley. Reinforced concrete and fiber reinforced concrete panels subjected to blast detonations and post-blast static tests. *Engineering Structures*, 76:24–33, 2014.

[23] D. Briccola, M. Ortiz, and A. Pandolfi. Experimental validation of metaconcrete blast mitigation properties. *Journal of Applied Mechanics*, 84, 2017.

[24] C. Wu, D.J. Oehlers, M. Rebentrost, J. Leach, and A.S. Whittaker. Blast testing of ultra-high performance fibre and FRP-retrofitted concrete slabs. *Engineering Structures*, 31:2060–2069, 2009.

[25] S. Astarlioglu and T. Krauthammer. Response of normal-strength and ultra-high-performance fiber-reinforced concrete columns to idealized blast loads. *Engineering Structures*, 61:1–12, 2014.

[26] J. Xu, C. Wu, H. Xiang, Y. Su, Z.-X. Li, Q. Fang, H. Hao, Z. Liu, Y. Zhang, and J. Li. Behaviour of ultra high performance reinforced concrete columns subjected to blast loading. *Engineering Structures*, 118:97–107, 2016.

[27] L. Mao, S.J. Barnett, A. Tyas, J. Warren, G.K. Schleyer, and S.S. Zaini. Response of small scale ultra high performance fibre reinforced concrete slabs to blast loading. *Construction and building materials*, 93:822–830, 2015.

[28] L. Soufeiani, S.N. Raman, M.Z.B. Jumaat, U.J. Alengaram, G. Ghadyani, and P. Mendis. Influences of the volume fraction and shape of steel fibers on fiber-reinforced concrete subjected to dynamic loading – A review. *Engineering Structures*, 124:405–417, 2016.

[29] M. Colombo, M. di Prisco, and P. Martinelli. A new shock tube facility for tunnel safety. *Experimental Mechanics*, 51:1143–1154, 2011.

[30] R. Andreotti, M. Colombo, and A. Guardone. Performance of a shock tube facility for impact response of structures. *International Journal of Non-Linear Mechanics*, 72:53–66, 2015.

[31] S.D. Adhikary, L.R. Chandra, A. Christian, and K.C.G. Ong. Influence of cylindrical charge orientation on the blast response of high strength concrete panels. *Engineering Structures*, 2016. Article in press. http://dx.doi.org/10.1016/j.engstruct.2016.04.035.

[32] F. Toutlemonde, C. Boulay, and C. Gourraud. Shock-tube tests of concrete slabs. *Materials and Structures*, 26:38–42, 1993.

[33] F. Toutlemonde, P. Rossi, C. Boulay, C. Gourraud, and D. Guedon. Dynamic behaviour of concrete: tests of slabs with a shock tube. *Materials and Structures*, 28:293–298, 1995.

[34] G. Thiagarajan, A.V. Kadambi, S. Robert, and C.F. Johnson. Experimental and finite element analysis of double reinforced concrete slabs under blast loads. *International Journal of Impact Engineering*, 75:162–173, 2015.

[35] L.E. Malvern, D.A. Jenkins, T. Tang, and C.A. Ross. Dynamic compressive testing of concrete. *Proceedings of 2nd symposium on the Interaction of Non-Nuclear Munitions with Structures*, pages 194–199, Florida, USA, 1985.

[36] J.C. Gong and L.E. Malvern. Passively confined tests of axial dynamic compressive strength of concrete. *Experimental Mechanics*, 30:55–59, 1990.
[37] P.H. Bischoff and S.H. Perry. Compressive behaviour of concrete at high strain rates. *Materials and Structures*, 24:425–450, 1991.
[38] D.L. Grote, S.W. Park, and M. Zhou. Dynamic behavior of concrete at high strain rates and pressures: I. experimental characterization. *International Journal of Impact Engineering*, 25:869–886, 2001.
[39] Q.M. Li and H. Meng. About the dynamic strength enhancement of concrete-like materials in a split Hopkinson pressure bar test. *International Journal of Solids and Structures*, 40:343–360, 2003.
[40] D.M. Cotsovos and M.N. Pavlović. Numerical investigation of concrete subjected to compressive impact loading. Part 1: A fundamental explanation for the apparent strength gain at high loading rates. *Computers and Structures*, 86:145–163, 2008.
[41] Y.B. Lu and Q.M. Li. About the dynamic uniaxial tensile strength of concrete-like materials. *International Journal of Impact Engineering*, 38:171–180, 2011.
[42] L. Chen, Q. Fang, X. Jiang, Z. Ruan, and J. Hong. Combined effects of high temperature and high strain rate on normal weight concrete. *International Journal of Impact Engineering*, 86:40–56, 2015.
[43] LSTC. *LS-Dyna Keyword User's Manual*. Livermore Software Technology Corporation, 2007.
[44] L.J. Malvar, J.E. Crawford, J.W. Wesewich, and D. Simons. A plasticity concrete material model for DYNA3D. *International Journal of Impact Engineering*, 19:847–873, 1997.
[45] J.M. Magallanes, Y. Wu, L.J. Malvar, and J.E. Crawford. Recent improvements to Release III of the K&C concrete model. *11th International LS-DYNA users conference, Michigan, USA*, 2010.
[46] Z. Tu and Y. Lu. Evaluation of typical concrete material models used in hydrocodes for dynamic response simulations. *International Journal of Impact Engineering*, 36:132–146, 2009.
[47] *NS-EN 12390-6: Testing hardened concrete – Part 6: Tensile splitting strength of test specimens*. Standard Norge, 2009.
[48] *NS-EN 1992-1-1: Design of concrete structures – Part 1-1: General rules and rules for buildings*. Standard Norge, 2004.
[49] *HB185: Bruprosjektering*. Statens Vegvesen, draft edition, 2013. `http://www.vegvesen.no/_attachment/544938/binary/876493`.
[50] *N400: Bruprosjektering*. Statens Vegvesen, 2015. `http://www.vegvesen.no/_attachment/865860/binary/1030718`.
[51] F. Casadei and J.P. Halleux. An algorithm for permanent fluid-structure interaction in explicit transient dynamics. *Computer Methods in Applied Mechanics and Engineering*, 128:231–289, 1995.
[52] E. Fagerholt. Cited 11.04.2018. `https://www.ntnu.edu/kt/ecorr`.
[53] R.C. Juvinall and K. Marshek. *Fundamentals of Machine Component Design*. Wiley, New York, 3rd edition, 2000. ISBN 0471244481.
[54] Y. Jiang, J. Chang, and C.-H. Lee. An experimental study of the torque-tension relationship for bolted joints. *International Journal of Materials & Product Technology*, 16:417–429, 2001.
[55] Y. Qu, X. Li, X. Kong, W. Zhang, and X. Wang. Numerical simulation on dynamic behavior of reinforced concrete beam with initial cracks subjected to air blast loading. *Engineering Structures*, 128:96–110, 2016.
[56] M. Kristoffersen, K. Osnes, S.R. Haug, V. Aune, and T. Børvik. Shock tube testing and numerical simulations of concrete slabs. *1st International Conference on Impact Loading of Structures and Materials*, Turin, Italy, 2016.
[57] T. Børvik, O.S. Hopperstad, and T. Berstad. On the influence of stress triaxiality and strain rate on the behaviour of a structural steel. Part II. Numerical study. *European Journal of Mechanics A/Solids*, 22:15–32, 2003.
[58] S. Dey, T. Børvik, X. Teng, T. Wierzbicki, and O.S. Hopperstad. On the ballistic resistance of double-layered steel plates: An experimental and numerical investigation. *International Journal of Solids and Structures*, 44:6701–6723, 2007.
[59] S.-J. Choi, S.-W. Lee, and J.-H. Jay Kim. Impact or blast induced fire simulation of bi-directional PSC panel considering concrete confinement and spalling effect. *Engineering Structures*, 2017. `http://dx.doi.org/10.1016/j.engstruct.2016.12.056`.
[60] P. Forquin, A. Arias, and R. Zaera. Role of porosity in controlling the mehcanical and impact behaviours of cement-based materials. *International Journal of Impact Engineering*, 35:133–146, 2008.
[61] P. Forquin, A. Arias, and R. Zaera. Relationship between mesostructure, mechanical behavior and damage of cement composites under high-pressure confinement. *Experimental Mechanics*, 49:613–625, 2009.
[62] P. Forquin, K. Safa, and G. Gary. Influence of free water on the quasi-static and dynamic strength of concrete in confined compression tests. *Cement and Concrete Research*, 40:321–333, 2010.
[63] Y.C. Fung. *Foundations of solid mechanics*. Prentice hall, 1965.
[64] B. Erzar and P. Forquin. Experiments and mesoscopic modelling of dynamic testing of concrete. *Mechanics of Materials*, 43:505–527, 2011.
[65] Z. Xu, H. Hao, and H.N. Li. Mesoscale modelling of fibre reinforced concrete material under compressive impact loading. *Construction and building materials*, 26:274–288, 2012.